Optically Modulated Ultra-Broad-Band Warm White Emission in Mn^{2+}-Doped (C$_6$H$_{18}$N$_2$O$_2$)PbBr$_4$ Hybrid Metal Halide Phosphor

Guojun Zhou,[†] Xingxing Jiang,[‡] Maxim Molokeev,[∥,⊥,#] Zheshuai Lin,[‡,§] Jing Zhao,[†] Jing Wang,[∇] and Zhiguo Xia*,[†,○]

[†]The Beijing Municipal Key Laboratory of New Energy Materials and Technologies, School of Materials Sciences and Engineering, University of Science and Technology Beijing, Beijing 100083, China

[‡]Technical Institute of Physics and Chemistry, Chinese Academy of Sciences, Beijing 100190, China

[§]University of Chinese Academy of Sciences, Beijing 100049, China

[∥]Laboratory of Crystal Physics, Kirensky Institute of Physics, Federal Research Center KSC SB RAS, Krasnoyarsk 660036, Russia

[⊥]Siberian Federal University, Krasnoyarsk 660041, Russia

[#]Department of Physics, Far Eastern State Transport University, Khabarovsk 680021, Russia

[∇]Ministry of Education Key Laboratory of Bioinorganic and Synthetic Chemistry, State Key Laboratory of Optoelectronic Materials and Technologies, School of Chemistry, School of Materials Science and Engineering, Sun Yat-Sen University, Guangzhou 510275, China

[○]State Key Laboratory of Luminescent Materials and Devices and Institute of Optical Communication Materials, South China University of Technology, Guangzhou 510641, China

S *Supporting Information*

ABSTRACT: Finding new low-dimensional metal halides with broad-band emission is attracting interest in single-component phosphor for white light-emitting diodes (WLEDs). The full-spectrum white light still remains a challenge as found in the two-dimensional hybrid material (C$_6$H$_{18}$N$_2$O$_2$)PbBr$_4$ exhibiting the intrinsic free exciton (FE) and broad-band self-trap exciton (STE) emission upon 365 nm ultraviolet excitation, and a combined strategy has been proposed through doping the Mn^{2+} ions enabling a super-position of multiple emission centers toward the ultra-broad-band warm white light. The occupation of Mn^{2+} in (C$_6$H$_{18}$N$_2$O$_2$)PbBr$_4$ has been discussed, and optical investigations verify that the warm white-light emission of Mn^{2+}-doped (C$_6$H$_{18}$N$_2$O$_2$)PbBr$_4$ originates from the coupling effects of the FE, STEs, and the $^4T_1-^6A_1$ transition of the doped Mn^{2+}. When the concentration of Mn^{2+} is 5%, the emission spectrum of the phosphor covers all visible-light areas with a full width at half maximum (FWHM) of about 230 nm. The high R_a (84.9) and warm light CCT (3577 K) values of the as-fabricated WLED lamp demonstrate that (C$_6$H$_{18}$N$_2$O$_2$)Pb$_{1-x}$Mn$_x$Br$_4$ can be promising as single-component white-light phosphor in solid-state lighting. Our work could provide a new understanding and perspective about hybrid metal halides for designing superior phosphor toward single-component white emission.
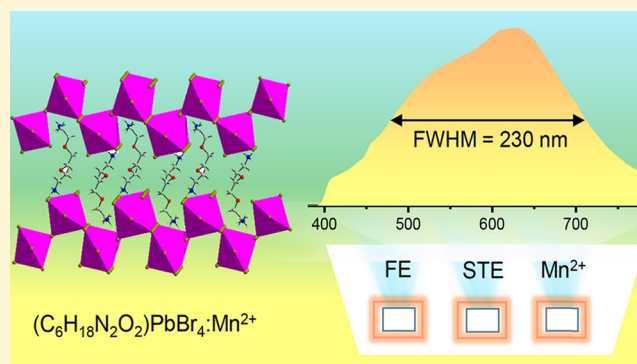
INTRODUCTION

Organic−inorganic hybrid metal halides are an interesting family of functional materials with the impressive structural diversity and the enormous applications in the fields of light-emitting diodes (LED),[1−3] solar cells,[4−6] photodetectors,[7−10] and so on. From the view of structural dimension, the configuration of the metal halide polyhedra can be divided into three- (3D), two- (2D), one- (1D), and zero-dimensional (0D) types by choosing suitable organic and inorganic components.[8,11−13] In particular, the recently discovered broad-band emission in the low-dimensional metal halides, such as 2D, 1D, and 0D materials, demonstrates a great

potential in the field of solid-state lighting.[12,14−18] Normally, the intrinsic broad-band emissions of low-dimensional materials arise from self-trap excitons (STEs)[16,18−21] or excitons trapped by controlled intrinsic vacancies.[22]

To date, the white-light sources can be achieved by covering multiple phosphors on commercial UV/blue chips, and the white LEDs (WLEDs) fabricated by several kinds of phosphors cause efficiency losses and poor color purity because of the
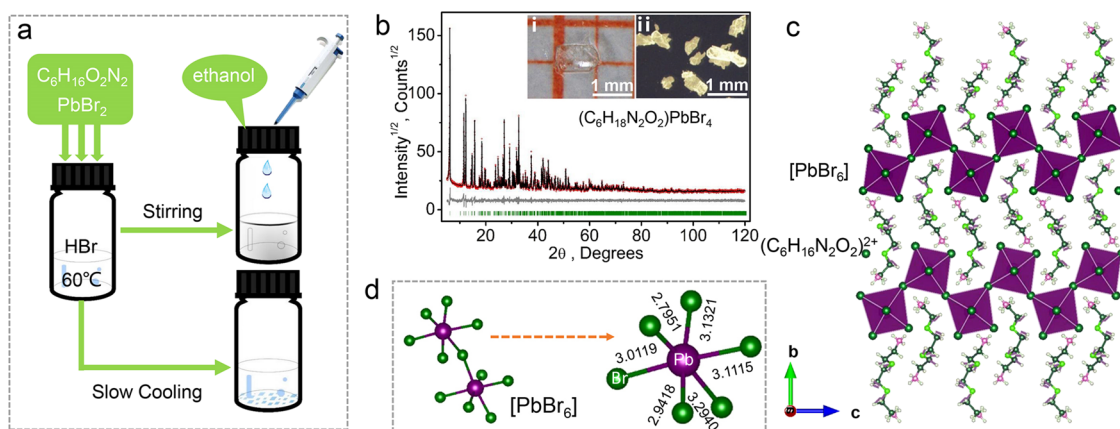
Figure 1. (a) Experimental illustration diagram for the synthesis of $(C_6H_{18}N_2O_2)PbBr_4$ via a chemical precipitation method. (b) Rietveld refinement result of $(C_6H_{18}N_2O_2)PbBr_4$ and the insets show the microscopy photographs of the single-crystal $(C_6H_{18}N_2O_2)PbBr_4$ under daylight and 365 nm UV excitation. (c) The structural diagram of 2D-layered $(C_6H_{18}N_2O_2)PbBr_4$. (d) Local structure of $[PbBr_6]$ polyhedra by sharing corners and local structure with different bond lengths.

self-absorption and different degradation rates during long-term operation. Accordingly, designing new single-component white-light-emitting phosphors for full-spectrum light is vital and important for high-performance WLEDs.[23] In particular, the low-dimensional metal halides are attracting interests due to the advantages such as easy-processing material, low cost, and high photoluminescence quantum yield. Importantly, unlike in purely inorganic solids, the organic—inorganic metal halides allow us to artificially design the connectivity of an inorganic lattice through choosing suitable organic components.[11,24−27] As a result, the broad-band emission with the large Stokes shift can be achieved in low-dimensional metal halides,[28] providing access to single-component phosphor with white emission. However, not every continuous spectral band of hybrid metal halides can perfectly cover the whole visible region. Thus, it prompts us to look for some activator ions to compensate for the lack of local fluorescence, which also plays a key role in improving the color-rendering index (R_a) and controlling the correlated color temperature (CCT).

It is well-known that divalent manganese (Mn^{2+}) is an important optically active luminescence ion with broad-band emission, other than rare-earth ions (Eu^{2+}, Ce^{3+}, etc.) and some transition-metal species (Bi^{2+}, Bi^{3+}, Ni^{2+}, etc.).[29,30] Up to now, the $^4T_1-^6A_1$ transitions of Mn^{2+} have been realized and extensively reported in 3D halide perovskites due to the host-to-dopant energy transfer.[31] Additionally, the Mn^{2+}-doped 2D hybrid perovskite with $A_2^IB^{II}X_4$ type can also achieve an efficient energy transfer due to the strong exciton binding energy, indicating that the doping of Mn^{2+} ions can realize high-efficient emission.[32,33] However, the Mn^{2+}-doped 2D hybrid perovskite with $A^{II}B^{II}X_4$ type has not been reported until now. Moreover, the broad-band emission is generally due to the recombination of free excitons (FE) and STE emission, and the tuning of the photoluminescence is still a challenge. In view of this, the coupling effects of the FE, STEs, and $^4T_1-^6A_1$ transition of Mn^{2+} can provide amusing optical properties as expected.

The 2D metal halide $(C_6H_{18}N_2O_2)PbBr_4$ has been previously reported as a white emitter combining the FE and STE emission.[14,18] Herein, the design principle on how to realize ultra-broad-band emission has been proposed, and one can find that the Mn^{2+}-doped $(C_6H_{18}N_2O_2)PbBr_4$ possess a full width at half maximum (FWHM) of 230 nm. Moreover,

the phase determination and photoluminescence properties of Mn^{2+}-doped $(C_6H_{18}N_2O_2)PbBr_4$ with broad-band emission have been investigated in detail. The ultra-broad-band warm white-light emission is attributed to the coupling effects of free excitons, self-trap excitons, and the $^4T_1-^6A_1$ transition of Mn^{2+} in one system. The design rules established here could allow us to systematically optimize white-light emission from low-dimensional metal halide by incorporating active luminescence ions.[12,34]

■ EXPERIMENTAL SECTION

Materials. $PbBr_2$ (99.9%, Aladdin), $C_6H_{16}N_2O_2$ (2,2′-(ethylenedioxy)bis(ethylamine), 98%, Macklin), C_2H_5OH (ethanol, 99.8%, Sinopharm), HBr (48% in water by weight, Aladdin), $MnBr_2$·$5H_2O$ (99.5%, Sinopharm). All chemicals were used as received.

Synthesis of $(C_6H_{18}N_2O_2)PbBr_4$. $C_6H_{16}N_2O_2$ (1 mmol) and $PbBr_2$ (1 mmol) were dissolved in 2 mL of HBr under vigorous stirring at 60 °C. After 1 h, the adequate ethanol was added to the above solution. The supernatant liquids were removed, and the polycrystalline samples were repeatedly washed using ethanol. Then, the samples were filtered and dried under vacuum at 70 °C overnight. Single crystals can be synthesized by slow crystallization (i.e., no addition of ethanol and slow evaporation).

Synthesis of $(C_6H_{18}N_2O_2)Pb_{1−x}Mn_xBr_4$. $MnBr_2$·$5H_2O$ was used as a Mn^{2+} source, and it was preheated to remove the crystal water at 120 °C. The desired amount of the above $(C_6H_{18}N_2O_2)PbBr_4$ was mixed with $MnBr_2$ in an agate mortar. The powder samples were thoroughly ground for several minutes and heated under vacuum at 115 °C for 2 h.

Characterization. The single-crystal X-ray diffraction data were collected by using an XtaLAB AFC12 X-ray four-circle single-crystal diffractometer (Rigaku) equipped with a CCD-detector, a graphite monochromator, and a Cu Kα radiation source. The powder X-ray diffraction patterns were collected by using a D8 Advance diffractometer (Bruker Corporation, Germany), operating at 40 kV and 40 mA with monochromatized Cu Kα radiation ($\lambda = 1.5406$ Å). The data used for the Rietveld analysis (2θ range 5−120°) was collected in a step-scanning mode with a step size of 0.02° and 5 s counting time per step. The Rietveld structure refinements were performed by using TOPAS 4.2. The morphology observation and elemental mapping were conducted by a scanning electron microscope (SEM, JEOL JSM-6510). Electron paramagnetic resonance (EPR) spectra were recorded by an electron paramagnetic resonance EPR spectrometer (Bruker, A300). The photoluminescence (PL), photoluminescence excitation (PLE) spectra, and luminescence decay curves were measured by a FLSP9200 fluorescence spectrophotom-

eter (Edinburgh Instruments Ltd., U. K.). The absorption spectra were collected by an UV−vis−NIR spectrophotometer (SolidSpec-3700 Shimadzu) with $BaSO_4$ serving as a reference standard. The photoluminescence quantum yields (PLQYs) were recorded by a commercialized PLQY measurement system from Ocean Optics with excitation from a 365 nm LED. For the WLED lamp fabrication, the near-UV LED chips (λ = 365 nm) were combined with $(C_6H_{18}N_2O_2)Pb_{1-x}Mn_xBr_4$ phosphors. The electroluminescence spectra, color-rendering index (R_a), and correlated color temperature (CCT) of the as-fabricated WLEDs were collected by an UV−vis−near-IR spectrophotocolorimeter (PMS-80, Everfine).

Computational Methods. The first-principle electronic structure calculation was carried out by CASTEP, a package based on plane-wave pseudo-potential density functional theory (DFT).[35] The exchange-correlation terms in the Hamiltonian method was described by the function developed by Ceperley, Alder, Perdew, and Zunger (CA-PZ)[36] in the local density approximation (LDA)[37] form. The effective interaction between the atomic cores and valence electrons was treated by optimized norm-conserving pseudopotentials, which allow us to employ a relatively small plane-wave basis set without compromising the computational accuracy. The kinetic energy cutoff 900 eV and intensive Monkhorst-Pack k-point meshes reaching less than $0.04/Å^3$ were chosen. One of the four plumbums was replaced by the manganese atom to model the Mn^{2+}-doped $(C_6H_{18}N_2O_2)$-$Pb_{0.75}Mn_{0.25}Br_4$. To account for the effect of the delocalized d orbitals in manganese atoms, The LDA+U method[38] was adopted in the calculation with the U_d set to 4.0 eV.

RESULTS AND DISCUSSION

The single-crystal products were grown from a slowly cooled hydrobromic acid solution, as illustrated in Figure 1a. When a certain amount of ethanol is gradually added to the above acid solution as an antisolvent, the pure $(C_6H_{18}N_2O_2)PbBr_4$ powder crystals are obtained. The insets of Figure 1b show the microscopy photographs of single crystals with a crystal size of about 1 mm and exhibit the yellow-white fluorescence upon 365 nm UV light. The crystal structure is characterized by the single-crystal X-ray diffraction technique, and the unit cell corresponds to the monoclinic symmetry. The space group $P2_1/c$ is determined from the statistical analysis of the intensities of all the reflections. The structure is solved by the direct methods using the SHELXS package and refined in the anisotropic approach for nonhydrogen atoms using SHELXL program.[39] The crystallographic information file (CIF) of $(C_6H_{18}N_2O_2)PbBr_4$ is demonstrated in the Supporting Information, and the main crystal data are shown in Table 1. The coordinates of atoms and main bond lengths

Table 1. Main Structure Parameters of and Crystallographic Data for $(C_6H_{18}N_2O_2)PbBr_4$

formula moiety	$(C_6H_{18}N_2O_2)PbBr_4$
molecular weight (g mol^{-1})	677.05
temperature (K)	150
space group (Z)	$P2_1/c$, 4
a (Å)	6.1145(1)
b (Å)	28.7310(5)
c (Å)	8.9259(2)
β (°)	91.487(2)
V (Å^3)	1567.54(5)
ρ_{calc} (g cm^{-3})	2.869
$2\theta_{max}$ (°)	73.81
R1 [$F_o > 4\sigma(F_o)$]	0.0226
wR2	0.0587
Goof	1.063

are shown in Tables S1 and S2, respectively. Accordingly, the $(C_6H_{18}N_2O_2)PbBr_4$ structural parameters defined by single-crystal analysis are used as a basis in Rietveld refinement of the powder pattern, as also shown in Figure 1b. The refinement is produced using program TOPAS 4.2.[40] As depicted in the Figure 1c, it shows the typical 2D-layered structure with several molecules of $C_6H_{18}N_2O_2$ and $[PbBr_6]$ octahedra. In total, the Pb^{2+} ion is coordinated by six Br^- ions and forms the $[PbBr_6]$ octahedra. These octahedra are linked with each other by nodes forming 2D layers and organic molecules $C_6H_{18}N_2O_2$ are deposited between such layers. Moreover, the structural analysis reveals eight intermolecular hydrogen bonds in which joint organic molecules connected with $[PbBr_6]$ to form a 3D net. Figure 1d highlights the coordination environment of the $[PbBr_6]$ octahedra, such as the bond length of Pb−Br. Thus, the distortion parameter (Δd) can be calculated by using the following equation

$$\Delta d = \left(\frac{1}{6}\right) \sum \left[\frac{d_n - d}{d}\right]^2$$

where d is the average Pb−Br bond length, and d_n is the individual Pb−Br bond length. It shows that $(C_6H_{18}N_2O_2)$-$PbBr_4$ has the obvious distortion (Δd = 26.58 × 10^{-4}), indicating the coexistence of free excitons and self-trapped excitons luminescence in a deformable lattice.[21,41] Enlightened by this, the synthesized products are belong to a 2D-layered metal halide with the general formula of $A^{II}B^{II}X_4$, which enable the intrinsic broad-band emission, as discussed in detail below.[16,42]

Normally, Mn^{2+} ion-doped 2D metal halides can provide amusing optical properties and has been studied in other systems.[32,43] The identification of Mn doping is first characterized by powder X-ray diffraction, elemental mapping, and electron paramagnetic resonance, respectively. Figure 2a shows the XRD patterns of $(C_6H_{18}N_2O_2)Pb_{1-x}Mn_xBr_4$ with various Mn^{2+} concentrations. Results of structural refinements reveal that the unit cell volumes tend to decrease with the increase of Mn^{2+}, as shown in Figure 2b. This verifies that the lattice positions of Pb^{2+} are gradually substituted by Mn^{2+} ions due to the smaller ion radii (IR) of Mn^{2+} (CN = 6, 0.67−0.83 Å) than Pb^{2+} (CN = 6, 1.19 Å). As shown in Figure S1, the Rietveld refinement XRD pattern of $(C_6H_{18}N_2O_2)$-$Pb_{0.8}Mn_{0.2}Br_4$ can prove that the highly doped sample also belongs to the pure phase. The elemental mapping images (Figure 2c) for Pb, Br, and Mn indicate that they are homogeneously dispersed. As shown in Figure 2d, we comparatively measured the X-band EPR spectra of the $(C_6H_{18}N_2O_2)PbBr_4$ and doped samples $(C_6H_{18}N_2O_2)$-$Pb_{1-x}Mn_xBr_4$ (x = 0.001, 0.01) at liquid nitrogen temperature. Normally, the sextet structure is masked by heavy broadening of the EPR peaks due to magnetic interactions between close lying Mn^{2+} ions.[44] Then, the samples with lower Mn concentrations were repeatedly tested, but the splitting peaks were not observed, which may be related to that the Mn ions tend to form cluster in 2D-layered metal halide.[22]

In addition, we perform DFT calculations to investigate the impurity formation energy of Mn^{2+} ions in $(C_6H_{18}N_2O_2)$-$PbBr_4$. It is generally known that the impurity formation energy (E_f) of a particular substitutional dopant is given by the following equation[45]

$$E_f = E(doped) - E(pure) + u_{Pb} - u_{Mn}$$
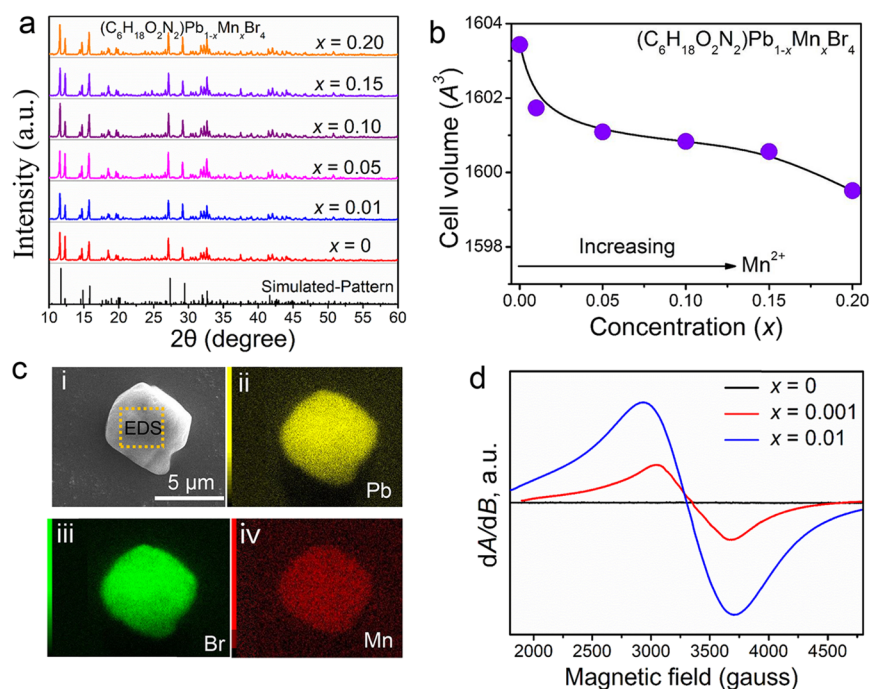
Figure 2. (a) XRD patterns of as-doped $(C_6H_{18}N_2O_2)Pb_{1-x}Mn_xBr_4$ (x = 0, 0.01, 0.05, 0.10, 0.15, 0.20). (b) Dependence of unit cell volumes on different Mn^{2+} doping concentrations. (c) SEM and elemental mapping images of Pb, Br, and Mn for the selected $(C_6H_{18}N_2O_2)Pb_{0.95}Mn_{0.05}Br_4$ particles. (d) Comparison of X-band EPR spectra on the host $(C_6H_{18}N_2O_2)PbBr_4$ and the doped sample $(C_6H_{18}N_2O_2)Pb_{1-x}Mn_xBr_4$ (x = 0.001, 0.01) at liquid nitrogen temperature.

where E(doped) and E(pure) are the total energies of $(C_6H_{18}N_2O_2)Pb_{0.75}Mn_{0.25}Br_4$ and $(C_6H_{18}N_2O_2)PbBr_4$, respectively. The chemical potentials u_{Mn} and u_{pb} are the substitutional Mn and Pb atoms, respectively. The calculated results are summarized in Table 2, and the formation energy E_f (eV)

Table 2. Total Energies (eV) of $(C_6H_{18}N_2O_2)PbBr_4$ and $(C_6H_{18}N_2O_2)Pb_{0.75}Mn_{0.25}Br_4$ as well as Chemical Potentials of Mn and Pb

model	total Energy (eV)
$(C_6H_{18}N_2O_2)PbBr_4$	−23074.03
$(C_6H_{18}N_2O_2)Pb_{0.75}Mn_{0.25}Br_4$	−21824.62
atom	chemical potential (eV)
Mn	−411.61
Pb	−1662.02

of $(C_6H_{18}N_2O_2)Pb_{0.75}Mn_{0.25}Br_4$ is −0.99 eV, which is substantially less than zero, indicating that the doped compound is easy to be formed and more stable than the pure one when manganese is contained, further verifying the successful incorporation of Mn^{2+} into $(C_6H_{18}N_2O_2)PbBr_4$.

Meanwhile, we comparatively investigated the optical properties of $(C_6H_{18}N_2O_2)PbBr_4$ and $(C_6H_{18}N_2O_2)$-$Pb_{1-x}Mn_xBr_4$. As can be seen from the normalized absorption, excitation, and emission spectra in Figure 3a, $(C_6H_{18}N_2O_2)$-$PbBr_4$ exhibits a broad emission band peaking at 403 and 555 nm upon 365 nm excitation. We assigned the peak at 403 nm as FE emission, and the broad-band emission at 555 nm with a large Stokes shift could be assigned as STE emission in a deformable lattice due to the strong electron-lattice coupling. With the doping of Mn^{2+} ions, the emission band of $(C_6H_{18}N_2O_2)Pb_{0.95}Mn_{0.05}Br_4$ becomes broadened with the appearance of the fluorescence peaking at about 640 nm, which

is attributed to the $^4T_1-^6A_1$ transition of Mn^{2+} due to an efficient energy-transfer effect in this system. In addition, the emission spectra as a function of the Mn^{2+} doping concentration in $(C_6H_{18}N_2O_2)Pb_{1-x}Mn_xBr_4$ (x = 0, 0.01, 0.05, 0.10, 0.15, 0.20) are exhibited in Figure 3b, indicating that the fluorescence spectrum covers all visible-light areas and the PL intensity peaking at 640 nm is enhanced with increasing Mn^{2+} concentration. When the concentration of Mn^{2+} is 5%, $(C_6H_{18}N_2O_2)Pb_{0.95}Mn_{0.05}Br_4$ achieves the ultra-broad-band warm white-light emission with a FWHM of 230 nm, as shown in Table 3. In addition, the PLQYs of the $(C_6H_{18}N_2O_2)Pb_{1-x}Mn_xBr_4$ (x = 0, 0.01, 0.05, 0.10, 0.15, 0.20) phosphors are 12.21, 12.34, 12.41, 12.54, 12.20, and 12.09%, respectively. Based on a comparison of the PLQY values with other hybrid perovskites with white-light emission,[46] it is found that the $(C_6H_{18}N_2O_2)Pb_{1-x}Mn_xBr_4$ phosphors possess the relatively high value. The photographs of $(C_6H_{18}N_2O_2)Pb_{1-x}Mn_xBr_4$ phosphors under daylight and 365 nm fluorescent light can also detect the change of emission colors (Figure 3c).

As a powerful evidence to certify the existence of multiple luminescence centers and understand the photophysical process, decay curves of $(C_6H_{18}N_2O_2)PbBr_4$ and $(C_6H_{18}N_2O_2)Pb_{0.95}Mn_{0.05}Br_4$ samples are measured at different monitoring wavelengths. As illustrated in Figure 3d, the PL decay curves monitored at λ_{em} = 403 and 555 nm are well fitted by a double exponential decay process with $I = A_1\exp(-t/\tau_1)+A_2\exp(-t/\tau_2)$, and the average lifetimes can be obtained by using the calculation formula $\tau = (A_1\tau_1^2 + A_2\tau_2^2)/(A_1\tau_1 + A_2\tau_2)$, corresponding to the 15.749 and 20.299 ns, which proves that the intrinsic broad-band emission of the 2D metal halide $(C_6H_{18}N_2O_2)PbBr_4$. The two emission peaks are believed to arise from free excitons and self-trap excitons, respectively.[14,21] Especially, the decay curve of $(C_6H_{18}N_2O_2)$-
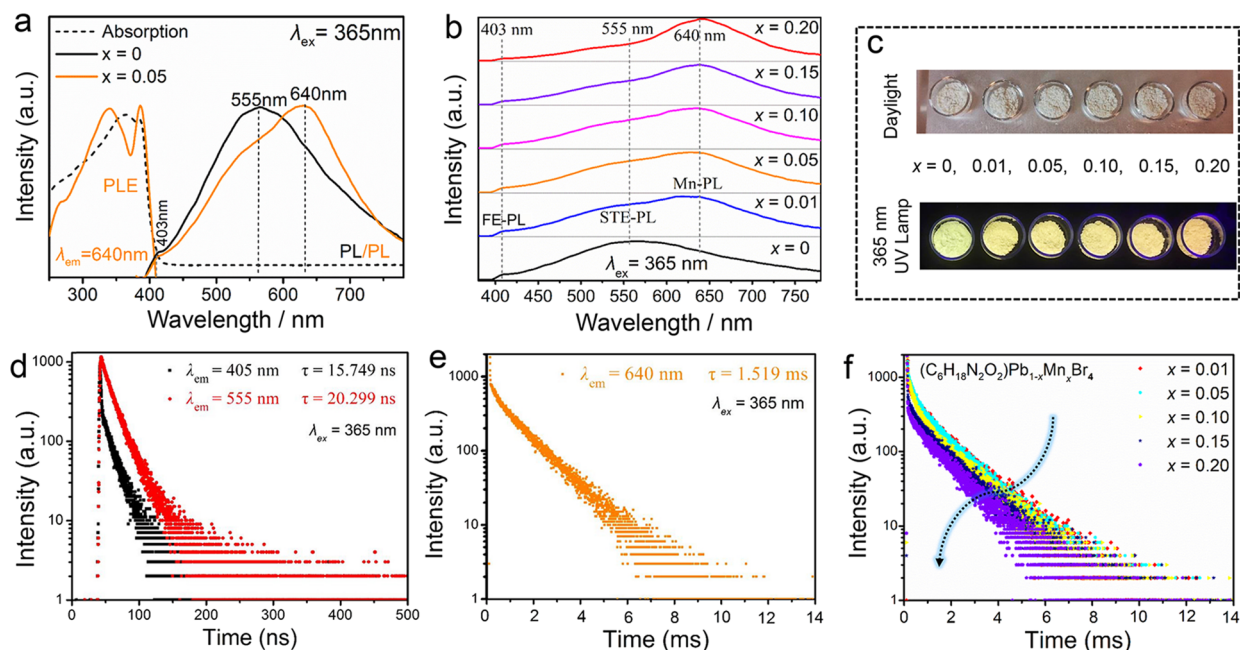
Figure 3. (a) Normalized absorption, excitation, and emission spectra of $(C_6H_{18}N_2O_2)Pb_{1-x}Mn_xBr_4$ (x = 0, 0.05). (b) The emission spectra of $(C_6H_{18}N_2O_2)Pb_{1-x}Mn_xBr_4$ under different Mn^{2+} concentrations. (c) The photographs of $(C_6H_{18}N_2O_2)Pb_{1-x}Mn_xBr_4$ phosphors under daylight and 365 nm UV lamp. (d) Decay curves of $(C_6H_{18}N_2O_2)Pb_{0.95}Mn_{0.05}Br_4$ under 365 nm excitation depending on emission wavelength at 403 and 555 nm. (e) The decay curve of $(C_6H_{18}N_2O_2)Pb_{0.95}Mn_{0.05}Br_4$ under excitation at 365 nm, monitored at 640 nm. (f) Decay curves of Mn^{2+} luminescence upon 365 nm excitation for $(C_6H_{18}N_2O_2)Pb_{1-x}Mn_xBr_4$ with different Mn concentrations.
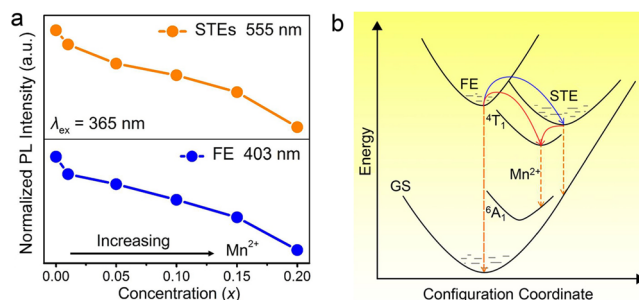
Table 3. FWHM Values and the Photoluminescence Quantum Yields of the Mn^{2+}-Doped Samples[a]

Mn^{2+} contents	FWHM (nm)	PLQY (%)	Mn^{2+} contents	FWHM (nm)	PLQY (%)
x = 0.05	182	12.21	x = 0.01	225	12.34
x = 0.05	230	12.41	x = 0.10	195	12.54
x = 0.15	180	12.20	x = 0.20	135	12.09

[a]$(C_6H_{18}N_2O_2)Pb_{1-x}Mn_xBr_4$ with x = 0, 0.01, 0.05, 0.10, 0.15, and 0.20.

Figure 4. (a) Variations of the normalized PL intensities of free excitons and self-trapping excitons emissions with increasing Mn^{2+} content. (b) Schematic diagram of different luminescence processes in $(C_6H_{18}N_2O_2)Pb_{1-x}Mn_xBr_4$ samples.

$Pb_{0.95}Mn_{0.05}Br_4$ monitored at 640 nm is illustrated in Figure 3e. The as-measured lifetime about 1.519 ms is obviously attributed to the $^4T_1-^6A_1$ transition of Mn^{2+}, which is consistent with the previous reports in Mn-doped metal halides.[32,33] This emission center perfectly complements the absence of red-light region, thus achieving the ultra-broad-band warm white-light emission in the single-component material. In Figure 3f, the lifetime values of Mn^{2+} tend to decrease with the increasing content of Mn^{2+} ions, indicating that the energy-transfer efficiency is enhanced in $(C_6H_{18}N_2O_2)Pb_{1-x}Mn_xBr_4$ (x = 0, 0.01, 0.05, 0.10, 0.15, 0.20). In addition, the normalized emission spectra of Mn^{2+}-doped samples were collected (Figure S2). As shown in Figure 4a, the decline trends of the normalized PL intensity produced by FE and STEs with an increase Mn^{2+} content are presented, indicating that the effective fluorescence of Mn^{2+} can be induced due to the energy transfers of FE-Mn^{2+} and STEs-Mn^{2+} in this system. Meanwhile, the energy-transfer efficiency (η_T) from the intrinsic emissions to the activator Mn^{2+} can be expressed as[34,47]

$$\eta_T = 1 - \frac{I_S}{I_{S0}}$$

where I_{S0} is the luminescence intensities of intrinsic emissions of the sample without Mn^{2+}, and I_S is the luminescence intensities of intrinsic emissions of the sample with Mn^{2+}. In the present $(C_6H_{18}N_2O_2)Pb_{1-x}Mn_xBr_4$ phosphors, the η_T values of FE-Mn^{2+} are determined to be 11.77, 20.29, 29.14, 40.95, and 63.12% with x = 0.01, 0.05, 0.1, 0.15, and 0.2. The η_T values of STEs-Mn^{2+} correspond to 8.63, 18.53, 27.41, 37.69, and 59.04%. As a consequence, the energy-transfer efficiency from the intrinsic emissions to the activator Mn^{2+} in this system increases gradually with increasing Mn^{2+} doping concentration, and the energy-transfer efficiency from free excitons to Mn^{2+} is similar as that from self-trapped excitons to Mn^{2+}. Initially, we give the schematic energy-level diagram of the luminescence process in $(C_6H_{18}N_2O_2)Pb_{1-x}Mn_xBr_4$ phosphors as presented in Figure 4b. Based on the above discussion, the ultra-broad-band warm white-light emission in this single-component system comes from the coupling effects of the free excitons, self-trap excitons, and $^4T_1-^6A_1$ transitions of Mn^{2+} emissions.

To further evaluate the optical properties and emission mechanisms of $(C_6H_{18}N_2O_2)Pb_{1-x}Mn_xBr_4$, the electronic band structure and densities of states (DOS) calculated with the density functional theory (DFT) are illustrated in Figure 5.
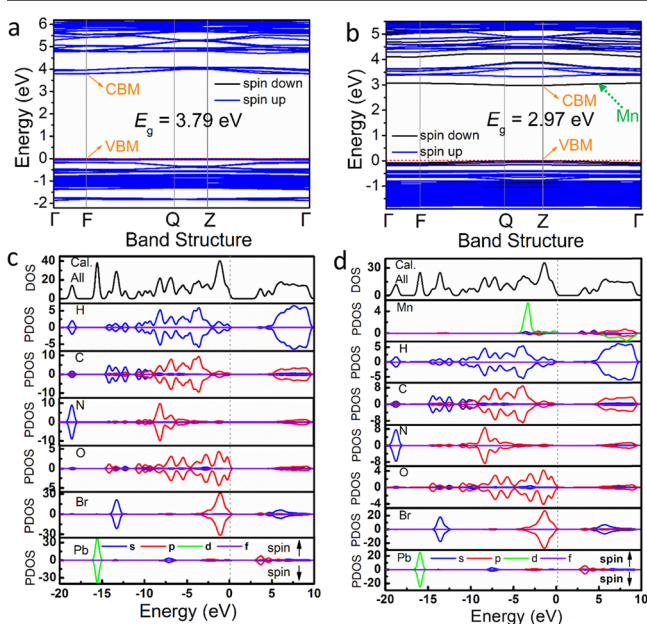
Figure 5. (a, b) Electronic band structures of the host $(C_6H_{18}N_2O_2)PbBr_4$ and the doped sample $(C_6H_{18}N_2O_2)Pb_{0.75}Mn_{0.25}Br_4$ calculated with the DFT-PBE method. (c, d) The total and orbital-projected partial density of states of $(C_6H_{18}N_2O_2)PbBr_4$ and $(C_6H_{18}N_2O_2)Pb_{0.75}Mn_{0.25}Br_4$ obtained with the DFT-PBE method.

The calculated band gap of $(C_6H_{18}N_2O_2)PbBr_4$ is 3.79 eV (Figure 5a); however, the band gap value of $(C_6H_{18}N_2O_2)$-$Pb_{0.75}Mn_{0.25}Br_4$ was reduced to 2.97 eV (Figure 5b). This band-gap-decreasing effect implies that the orbital of manganese would be located near the energy levels around forbidden bands. Figure 5c,d displays the partial density of states (PDOS) projected onto the constituent elements in $(C_6H_{18}N_2O_2)PbBr_4$ and $(C_6H_{18}N_2O_2)Pb_{0.75}Mn_{0.25}Br_4$, respectively. Accordingly, only the inorganic part contributes both the top of the valence bands and bottom of conduction bands in $(C_6H_{18}N_2O_2)PbBr_4$. This confirmed that the fluorescence emission resulted from self-trap excitons mainly occurs within the $[PbBr_6]$ octahedra. In $(C_6H_{18}N_2O_2)Pb_{0.75}Mn_{0.25}Br_4$, it is observed that the Mn 3d orbitals emerge at the top of the valence bands, and the bottom of the conduction bands is dominantly occupied by Mn 4s orbitals, while the position of the orbitals in plumbum and bromine in the electronic structure keeps almost unchanged. This demonstrated that the Mn^{2+} ions introduce new fluorescence emission wavelength on the prerequisite of not affecting the peak position of intrinsic emission and hence resulted in the ultra-broad-band white-light emission.

As discussed above, the ultra-broad-band emission of $(C_6H_{18}N_2O_2)Pb_{0.95}Mn_{0.05}Br_4$ phosphor nearly covers the whole visible-light range. To further verify the full-spectrum emission of $(C_6H_{18}N_2O_2)Pb_{1-x}Mn_xBr_4$ in the application of solid-state lighting, a series of WLEDs lamps were assembled by coating the selected samples of $(C_6H_{18}N_2O_2)PbBr_4$ and $(C_6H_{18}N_2O_2)Pb_{0.95}Mn_{0.05}Br_4$ on the 365 nm UV LED chips. Figure 6a shows the CIE chromaticity coordinates of $(C_6H_{18}N_2O_2)Pb_{1-x}Mn_xBr_4$ phosphors (x = 0, 0.01, 0.05,
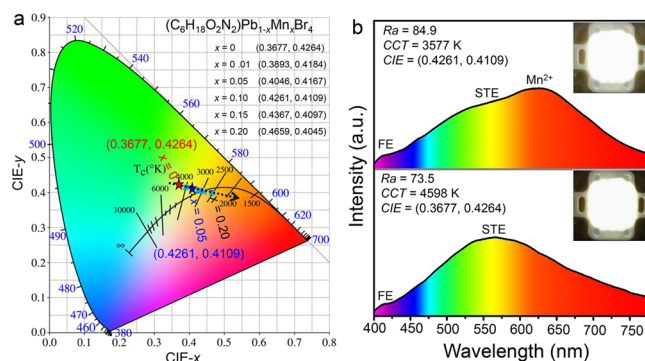
Figure 6. (a) CIE chromaticity coordinates of $(C_6H_{18}N_2O_2)$-$Pb_{1-x}Mn_xBr_4$ phosphors (x = 0, 0.01, 0.05, 0.10, 0.15, 0.20) and the fabricated WLEDs. (b) Photographs and emission spectra of WLEDs fabricated by $(C_6H_{18}N_2O_2)PbBr_4$ and $(C_6H_{18}N_2O_2)$-$Pb_{0.95}Mn_{0.05}Br_4$ phosphors driven by a UV chip (λ_{em} = 365 nm).

0.10, 0.15, 0.20) and the fabricated WLEDs lamps. The digital photographs, emission spectra, and optical parameters including the CIE coordinate, correlated color temperature (CCT), and color-rendering index (R_a) of the as-fabricated WLEDs are displayed in Figure 6b. It revealed the white emission with a CIE color coordinate of (0.4261, 0.4109), the warm white light with a CCT of 3577 K, and a color-rendering index (R_a) of 84.9, indicating that the high-quality WLEDs can be achieved by incorporating Mn^{2+} ions into the single-component $(C_6H_{18}N_2O_2)PbBr_4$ phosphor. In addition, with increasing drive currents, the normalized integrated intensity of emission spectra increases, and the luminous efficiency decreases gradually (Figure S3). Importantly, the color-rendering index is obviously improved when the Mn^{2+} ions are doped, and the R_a reflecting color restoration ability of the WLEDs in the deep-red region elevates from −26.3 to 32.4, also suggesting the importance of Mn^{2+} incorporation enabling warm white-light emission.

■ CONCLUSIONS

In summary, we have first developed the design principle to realize the ultra-broad-band warm white-light emission from the coupling effects of free excitons, self-trap excitons, and the $^4T_1$–$^6A_1$ transition of Mn^{2+} emissions in one system. Since the Mn^{2+} emission can compensate for the lack of red-light region, new Mn^{2+}-doped $(C_6H_{18}N_2O_2)Pb_{1-x}Mn_xBr_4$ with ultra-broad-band warm white-light emission has been reported. The incorporation of Mn^{2+} into $(C_6H_{18}N_2O_2)PbBr_4$ and the site occupation have been verified, and the fluorescence spectrum of $(C_6H_{18}N_2O_2)Pb_{0.95}Mn_{0.05}Br_4$ covers whole visible-light areas with a FWHM of 230 nm. The high R_a (84.9) and low CCT (3577 K) values of the as-fabricated WLEDs lamp verify that $(C_6H_{18}N_2O_2)Pb_{0.95}Mn_{0.05}Br_4$ can be promising as a single-component white-light phosphor in solid-state lighting. Our realizable cases could provide a new perspective for designing superior phosphor toward single-component white-emission in the doped low-dimensional metal halides.

■ ASSOCIATED CONTENT

ⓢ Supporting Information

The Supporting Information is available free of charge on the ACS Publications website at DOI: 10.1021/acs.chemmater.9b01864.

Rietveld refinement XRD pattern and normalized emission spectra of $(C_6H_{18}N_2O_2)Pb_{0.8}Mn_{0.2}Br_4$ and drive current-dependent normalized integrated intensity and luminous efficiency of LEDs devices; fractional atomic coordinates and isotropic or equivalent isotropic displacement parameters and hydrogen-bond geometry of some mentioned compounds (PDF)

Crystallographic information of $(C_6H_{18}N_2O_2)PbBr_4$ (CIF)

■ AUTHOR INFORMATION

Corresponding Author

*E-mail: xiazg@scut.edu.cn.

ORCID ⊙

Xingxing Jiang: 0000-0001-6068-8773
Zheshuai Lin: 0000-0002-9829-9893
Jing Zhao: 0000-0002-8000-5973
Jing Wang: 0000-0002-1246-991X
Zhiguo Xia: 0000-0002-9670-3223

Notes

The authors declare no competing financial interest.

■ REFERENCES

(1) Pathak, S.; Sakai, N.; Wisnivesky Rocca Rivarola, F.; Stranks, S. D.; Liu, J.; Eperon, G. E.; Ducati, C.; Wojciechowski, K.; Griffiths, J. T.; Haghighirad, A. A.; Pellaroque, A.; Friend, R. H.; Snaith, H. J. Perovskite crystals for tunable white light emission. *Chem. Mater.* **2015**, *27*, 8066−8075.

(2) Dou, L.; Wong, A. B.; Yu, Y.; Lai, M.; Kornienko, N.; Eaton, S. W.; Fu, A.; Bischak, C. G.; Ma, J.; Ding, T.; Ginsberg, N. S.; Wang, L. W.; Alivisatos, A. P.; Yang, P. D. Atomically thin two-dimensional organic-inorganic hybrid perovskites. *Science* **2015**, *349*, 1518.

(3) Tian, Y.; Zhou, C.; Worku, M.; Wang, X.; Ling, Y.; Gao, H.; Zhou, Y.; Miao, Y.; Guan, J.; Ma, B. Highly efficient spectrally stable red perovskite light-emitting diodes. *Adv. Mater.* **2018**, *30*, 1707093.

(4) Mao, L.; Ke, W.; Pedesseau, L.; Wu, Y.; Katan, C.; Even, J.; Wasielewski, M. R.; Stoumpos, C. C.; Kanatzidis, M. G. Hybrid dion-jacobson 2D lead Iodide perovskites. *J. Am. Chem. Soc.* **2018**, *140*, 3775−3783.

(5) Cao, D. H.; Stoumpos, C. C.; Farha, O. K.; Hupp, J. T.; Kanatzidis, M. G. 2D homologous perovskites as light-absorbing materials for solar cell applications. *J. Am. Chem. Soc.* **2015**, *137*, 7843−7850.

(6) Fu, W.; Wang, J.; Zuo, L.; Gao, K.; Liu, F.; Ginger, D. S.; Jen, A. K. Y. Two-dimensional perovskite solar cells with 14.1% power conversion efficiency and 0.68% external radiative efficiency. *ACS Energy Lett.* **2018**, *3*, 2086−2093.

(7) Li, L.; Sun, Z.; Wang, P.; Hu, W. D.; Wang, S. S.; Ji, C.; Hong, M.; Luo, J. Tailored engineering of an unusual $(C_4H_9NH_3)_2(CH_3NH_3)_2Pb_3Br_{10}$ Two-Dimensional multilayered perovskite ferroelectric for a High-Performance photodetector. *Angew. Chem. Int. Ed.* **2017**, *56*, 12150−12154.

(8) Chen, P.; Bai, Y.; Lyu, M.; Yun, J. H.; Hao, M.; Wang, L. Progress and perspective in low-dimensional metal halide perovskites for optoelectronic applications. *Solar. RRL.* **2018**, *2*, 1700186.

(9) Ding, J.; Du, S.; Zuo, Z.; Zhao, Y.; Cui, H.; Zhan, X. High detectivity and rapid response in perovskite $CsPbBr_3$ Single-Crystal photodetector. *J. Phys. Chem. C* **2017**, *121*, 4917−4923.

(10) Ding, J.; Cheng, X.; Jing, L.; Zhou, T.; Zhao, Y.; Du, S. Polarization-dependent optoelectronic performances in hybrid halide perovskite $MAPbX_3$ (X = Br, Cl) single-crystal photodetectors. *ACS Appl. Mater. Interfaces* **2017**, *10*, 845−850.

(11) Zhou, C.; Lin, H.; Lee, S.; Chaaban, M.; Ma, B. Organic−inorganic metal halide hybrids beyond perovskites. *Mater. Res. Lett.* **2018**, *6*, 552−569.

(12) Wu, G.; Zhou, C.; Ming, W.; Han, D.; Chen, S.; Yang, D.; Besara, T.; Neu, J.; Siegrist, T.; Du, M. H.; Ma, B.; Dong, A. A one-dimensional organic lead chloride hybrid with excitation-dependent broadband emissions. *ACS Energy Lett.* **2018**, *3*, 1443−1449.

(13) Zhou, C.; Lin, H.; Shi, H.; Tian, Y.; Pak, C.; Shatruk, M.; Zhou, Y.; Djurovich, P.; Du, M. H.; Ma, B. A zero-dimensional organic seesaw-shaped tin bromide with highly efficient strongly stokes-shifted deep-red emission. *Angew. Chem. Int. Ed.* **2018**, *57*, 1021−1024.

(14) Yuan, Z.; Zhou, C.; Messier, J.; Tian, Y.; Shu, Y.; Wang, J.; Xin, Y.; Ma, B. A microscale perovskite as single component broadband phosphor for downconversion white-light-emitting devices. *Adv. Opt. Mater.* **2016**, *4*, 2009−2015.

(15) Smith, M. D.; Jaffe, A.; Dohner, E. R.; Lindenberg, A. M.; Karunadasa, H. I. Structural origins of broadband emission from layered Pb-Br hybrid perovskites. *Chem. Sci.* **2017**, *8*, 4497−4504.

(16) Mao, L.; Wu, Y.; Stoumpos, C. C.; Wasielewski, M. R.; Kanatzidis, M. G. White-light emission and structural distortion in new corrugated two-dimensional lead bromide perovskites. *J. Am. Chem. Soc.* **2017**, *139*, 5210−5215.

(17) Dohner, E. R.; Hoke, E. T.; Karunadasa, H. I. Self-assembly of broadband white-light emitters. *J. Am. Chem. Soc.* **2014**, *136*, 1718−1721.

(18) Dohner, E. R.; Jaffe, A.; Bradshaw, L. R.; Karunadasa, H. I. Intrinsic white-light emission from layered hybrid perovskites. *J. Am. Chem. Soc.* **2014**, *136*, 13154−13157.

(19) Yangui, A.; Garrot, D.; Lauret, J. S.; Lusson, A.; Bouchez, G.; Deleporte, E.; Pillet, S.; Bendeif, E. E.; Castro, M.; Triki, S.; Abid, Y.; Boukheddaden, K. Optical investigation of broadband white-light emission in self-assembled organic−inorganic perovskite $(C_6H_{11}NH_3)_2PbBr_4$. *J. Phys. Chem. C* **2015**, *119*, 23638−23647.

(20) Hu, T.; Smith, M. D.; Dohner, E. R.; Sher, M. J.; Wu, X.; Trinh, M. T.; Fisher, A.; Corbett, J.; Zhu, X. Y.; Karunadasa, H. I.; Lindenberg, A. M. Mechanism for broadband white-light emission from two-dimensional (110) hybrid perovskites. *J. Phys. Chem. Lett.* **2016**, *7*, 2258−2263.

(21) Smith, M. D.; Karunadasa, H. I. White-light emission from layered halide perovskites. *Acc. Chem. Res.* **2018**, *51*, 619−627.

(22) Zhou, J.; Li, M.; Ning, L.; Zhang, R.; Molokeev, M.; Zhao, J.; Yang, S.; Han, K. L.; Xia, Z. Broad-band emission in a zero-dimensional hybrid organic $[PbBr_6]$ trimer with intrinsic vacancies. *J. Phys. Chem. Lett.* **2019**, *10*, 1337−1341.

(23) Zhao, M.; Liao, H. X.; Molokeev, M. S.; Zhou, Y. Y.; Zhang, Q. Y.; Liu, Q. L.; Xia, Z. G. Emerging ultra-narrow-band cyan-emitting phosphor for white LEDs with enhanced color rendition. *Light. Sci. Appl.* **2019**, *8*, 38.

(24) Stoumpos, C. C.; Mao, L.; Malliakas, C. D.; Kanatzidis, M. G. Structure-band gap relationships in hexagonal polytypes and low-dimensional structures of hybrid tin iodide perovskites. *Inorg. Chem.* **2016**, *56*, 56−73.

(25) Mao, L.; Guo, P.; Kepenekian, M.; Hadar, I.; Katan, C.; Even, J.; Schaller, R. D.; Stoumpos, C. C.; Kanatzidis, M. G. Structural diversity in white-light emitting hybrid lead bromide perovskites. *J. Am. Chem. Soc.* **2018**, *140*, 13078−13088.

(26) Hu, H.; Meier, F.; Zhao, D.; Abe, Y.; Gao, Y.; Chen, B.; Salim, T.; Chia, E. E. M.; Qiao, X.; Deibel, C.; Lam, Y. M. Efficient room-temperature phosphorescence from organic-inorganic hybrid perovskites by molecular engineering. *Adv. Mater.* **2018**, *30*, 1707621.

(27) Zhao, L.; Lin, Y. L.; Kim, H.; Giebink, N. C.; Rand, B. P. Donor/acceptor charge-transfer states at two-dimensional metal

halide perovskite and organic semiconductor interfaces. *ACS Energy Lett.* **2018**, *3*, 2708−2712.

(28) Smith, M. D.; Watson, B. L.; Dauskardt, R. H.; Karunadasa, H. I. Broadband emission with a massive stokes shift from sulfonium Pb−Br hybrids. *Chem. Mater.* **2017**, *29*, 7083−7087.

(29) Zhou, G.; Jiang, X.; Zhao, J.; Molokeev, M.; Lin, Z.; Liu, Q.; Xia, Z. Two-dimensional-layered perovskite $ALaTa_2O_7$:Bi^{3+} (A = K and Na) phosphors with versatile structures and tunable photoluminescence. *ACS Appl. Mater. Interfaces* **2018**, *10*, 24648−24655.

(30) Dai, P. P.; Li, C.; Zhang, X. T.; Xu, J.; Chen, X.; Wang, X. L.; Jia, Y.; Wang, X.; Liu, Y. C. A single Eu^{2+}-activated high-color-rendering oxychloride white-light phosphor for white-light-emitting diodes. *Light. Sci. Appl.* **2016**, *5*, e16024.

(31) Liu, W.; Lin, Q.; Li, H.; Wu, K.; Robel, I.; Pietryga, J. M.; Klimov, V. I. Mn^{2+}-doped lead halide perovskite nanocrystals with dual-color emission controlled by halide content. *J. Am. Chem. Soc.* **2016**, *138*, 14954−14961.

(32) Biswas, A.; Bakthavatsalam, R.; Kundu, J. Efficient exciton to dopant energy transfer in Mn^{2+}-doped $(C_4H_9NH_3)_2$ $PbBr_4$ Two-Dimensional (2D) layered perovskites. *Chem. Mater.* **2017**, *29*, 7816−7825.

(33) Bakthavatsalam, R.; Biswas, A.; Chakali, M.; Bangal, P. R.; Kore, B. P.; Kundu, J. Temperature-dependent photoluminescence and energy-transfer dynamics in Mn^{2+}-doped $(C_4H_9NH_3)_2$ $PbBr_4$ Two-Dimensional (2D) layered perovskite. *J. Phys. Chem. C* **2019**, *123*, 4739−4748.

(34) Wu, W.; Xia, Z. Synthesis and color-tunable luminescence properties of Eu^{2+} and Mn^{2+}-activated $Ca_3Mg_3(PO_4)_4$ phosphor for solid state lighting. *RSC Adv.* **2013**, *3*, 6051−6057.

(35) Clark, S. J.; Segall, M. D.; Pickard, C. J.; Hasnip, P. J.; Probert, M. I.; Refson, K.; Payne, M. C. First principles methods using CASTEP. *Z. Kristallogr.* **2005**, *220*, 567−570.

(36) Ceperley, D. M.; Alder, B. J. Ground state of the electron gas by a stochastic method. *Phys. Rev. Let.* **1980**, *45*, 566−569.

(37) Perdew, J. P.; Zunger, A. Self-interaction correction to density-functional approximations for many-electron systems. *Phys. Rev. B* **1981**, *23*, 5048−5079.

(38) Cococcioni, M.; de Gironcoli, S. Linear response approach to the calculation of the effective interaction parameters in the LDA+U method. *Phys. Rev. B* **2005**, *71*, No. 035105.

(39) Sheldrick, G. M. Crystal structure refinement with SHELXL. *Acta. Crystallogr. C. Struct. Chem.* **2015**, *71*, 3−8.

(40) Bruker. *Topas, version 4*: General profile and structure analysis software for powder diffraction data. Bruker AXS: Karlsruhe, Germany, 2008.

(41) Cai, P.; Wang, X.; Seo, H. J.; Yan, X. Bluish-white-light-emitting diodes based on two-dimensional lead halide perovskite $(C_6H_5C_2H_4NH_3)_2PbCl_2Br_2$. *Appl. Phys. Lett.* **2018**, *112*, 153901.

(42) Wu, Z.; Ji, C.; Sun, Z.; Wang, S.; Zhao, S.; Zhang, W.; Li, L.; Luo, J. Broadband white-light emission with a high color rendering index in a two-dimensional organic−inorganic hybrid perovskite. *J. Mater. Chem. C* **2018**, *6*, 1171−1175.

(43) Guria, A. K.; Dutta, S. K.; Das Adhikari, S.; Pradhan, N. Doping Mn^{2+} in lead halide perovskite nanocrystals: successes and challenges. *ACS Energy Lett.* **2017**, *2*, 1014−1021.

(44) Nandha, N.; Nag, A. Synthesis and luminescence of Mn-doped Cs2AgInCl6double perovskites. *Chem. Commun.* **2018**, *54*, 5205−5208.

(45) Guo, S.; Wang, Y.; Wang, C.; Tang, Z.; Zhang, J. Large spin-orbit splitting in the conduction band of halogen (F, Cl, Br, and I) doped monolayerWS2with spin-orbit coupling. *Phys. Rev. B* **2017**, *96*, 245305.

(46) Smith, M. D.; Connor, B. A.; Karunadasa, H. I. Tuning the luminescence of layered halide perovskites. *Chem. Rev.* **2019**, *119*, 3104−3139.

(47) Paulose, P. I.; Jose, G.; Thomas, V.; Unnikrishnan, N. V.; Warrier, M. K. R. Sensitized fluorescence of Ce^{3+}/Mn^{2+} system in phosphate glass. *J. Phys. Chem. Solids* **2003**, *64*, 841−846.